

# Voltage-tunable dual-colour quantum Bragg mirror detector (QBMD)

Germano M. Penello<sup>1,3</sup> , Pedro H. Pereira<sup>2,3\*</sup> , Vitor B. Sousa<sup>2,3</sup>, Rudy M. S. Kawabata<sup>2,3</sup>,  
Mauricio P. Pires<sup>1,3</sup>, Patricia L. Souza<sup>2,3</sup>

<sup>1</sup>Instituto de Física, Universidade Federal do Rio de Janeiro, R. Athos Silveira Ramos 149, Rio de Janeiro 21941-909, Brasil

<sup>2</sup>LabSem/CETUC, Pontifícia Universidade Católica do Rio de Janeiro, R. Marquês de São Vicente 124, Gávea, Rio de Janeiro 22451-040, Brasil

<sup>3</sup>DISSE, Instituto Nacional de Ciência e Tecnologia de Nanodispositivos Semicondutores, R. Marquês de São Vicente 225, Gávea, Rio de Janeiro, 22451-900, Brasil

## Article info

### Article history:

Received 14 Oct. 2022

Received in revised form 15 Dec. 2022

Accepted 19 Dec. 2022

Available on-line dd mm 2023

### Keywords:

Bound states in the continuum; intersubband transition; infrared detector; quantum Bragg mirror and dual-colour detection.

## Abstract

The electronic quasi-bound state in the continuum concept is explored in an InGaAs/InAlAs heterostructure to create a voltage-tunable dual-colour quantum Bragg mirror detector. This heterostructure is based on one main quantum well embedded between two different superlattices. By bandgap engineering, each superlattice gives rise to quasi-bound states in the continuum with a preferential direction for electron extraction. Due to these states, the photovoltaic photocurrent presents a dual-colour response, one in a positive direction at 340 meV (3.6  $\mu\text{m}$ ), and one in a negative direction at 430 meV (2.9  $\mu\text{m}$ ). The simultaneous dual-colour detection can be switched to a single-colour detection (340 meV or 430 meV) by applying a bias voltage. At 77 K, the specific detectivity for simultaneous dual-colour is  $2.5 \cdot 10^8$  Jones, while the single-colour detectivities are  $2.6 \cdot 10^9$  Jones at +2.0 V and  $7.7 \cdot 10^8$  Jones at -1.6 V for 340 meV and 430 meV, respectively.

## 1. Introduction

Bound state in the continuum (BIC) is an eigenmode embedded in the continuum spectrum observed in many wave systems, such as optical, acoustic, aquatic or quantum systems [1]. Even though the BIC lies inside the continuum, it is a localised state without leak channels to the continuum (nonradiative states). The BIC is widely explored in photonic applications that demand optical cavities with extremely high-quality factors [2], for example, biosensors [3], nonlinear optics [4], lasers [5], THz sensors [6, 7], and wireless power transfer [8].

The BIC was initially proposed in quantum mechanics by von Neumann and Wigner as a possible solution of the Schrödinger equation for periodic potentials [9]. Thanks to the mature epitaxial technology of III-V semiconductors, it is possible to grow complex heterostructures with such periodic potentials required to create electronic BICs. In 1992, Capasso *et al.* observed the electronic BIC in an

InGaAs/InAlAs heterostructure composed of a main quantum well surrounded by two superlattices [10]. These superlattices were carefully adjusted to work as quantum Bragg mirrors to turn a resonant state into the electronic BIC by quantum interferences of the electronic wavefunctions.

The use of electronic BIC for photodetection has potential to overcome some limitations presented in standard quantum well-infrared photodetectors (QWIPs), namely, the energy detection is not limited by the conduction band offset anymore, and it is possible to obtain higher operating temperatures due to decreased dark current. The operation of a photodetector with a BIC created by a symmetric heterostructure is depicted in Fig. 1. The electron initially in the ground state (black line) absorbs one photon (red arrow) and is promoted via optical transition (green arrow) to the bound state in the continuum (black line above the potential barrier). In the continuum states, the electron will flow to the left or to the right side (blue arrows) to reach the contact layers (not shown here) to generate a photocurrent signal. The optical transition

\*Corresponding author at: [pedro.hpereira@cetuc.puc-rio.br](mailto:pedro.hpereira@cetuc.puc-rio.br)

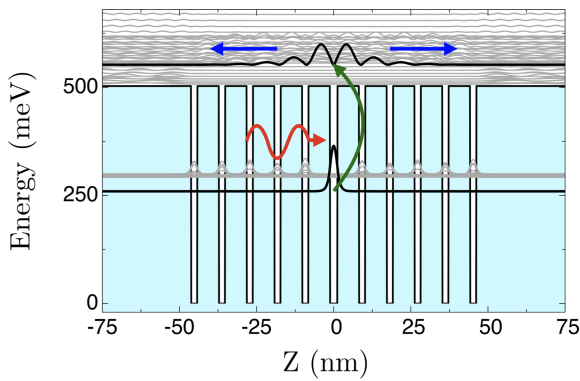


**Fig. 1.** The processes involved in the operation of the QBMD. The electron is excited from the ground state to the BIC (green arrow) by absorbing one photon (red arrow). When coupled with extended states in the continuum, this electron can flow to the left or right side (blue arrows) to generate a photocurrent signal.

between the bound state and the BIC provides an oscillator strength and a linewidth similar to a bound-to-bound transition [11, 12], but the bound-to-BIC transition has the advantage that the energy difference can be higher than the conduction band offset.

On the other hand, photodetectors based on BIC states using symmetric superlattices can only operate under applied bias voltage (photoconductive mode) [11] because the BIC cannot generate photocurrent (nonradiative state), so it should be turned into a quasi-BIC (leaky electronic state) by breaking the translational symmetry with an applied bias voltage. The quasi-BIC presents a wavefunction almost confined with a non-zero leaky rate, allowing the electron to be extracted and therefore generating a photocurrent. The second approach to create a quasi-BIC is using an asymmetric superlattice. In this case, the wavefunction is fully confined in one direction and partially confined in the other. This quasi-BIC has a preferential direction for the electron extraction even with a null applied bias voltage, which means that this photodetector can operate in photovoltaic mode [13]. This mode presents the lowest dark current [14], which directly influences the photodetector operation temperature. Using an asymmetric heterostructure, a photovoltaic device detecting 4.3  $\mu\text{m}$  (for  $\text{CO}_2$  fingerprint) operating at room temperature was developed [15]. Since the heterostructures of these devices are completely distinct from a QWIP [16] or a quantum cascade detector (QCD) [17], this new class of photodetectors, that explores optical transitions to electronic BICs or quasi-BICs, will be referred to as a quantum Bragg mirror detector (QBMD).

To show how tailorable quasi-BICs are for photodetectors, the authors explore their properties to develop a novel dual-colour QBMD that can simultaneously and distinctively detect two wavelength ranges under no applied bias (photovoltaic mode) or select which wavelength range to detect by applying positive or negative bias voltage (photoconductive mode). These combined features are particularly unachievable with a standard QWIP. To reach the simultaneous dual-colour response, the heterostructure is composed of two different superlattices surrounding the main quantum well. This heterostructure presents two quasi-BICs with different preferential directions for electronic extraction.

## 2. Heterostructure design and device fabrication

The QBMD sample was designed to generate a photovoltaic photocurrent with a dual-colour detection of around 310 meV (4.0  $\mu\text{m}$ ) and 430 meV (2.9  $\mu\text{m}$ ) by using an  $\text{In}_{0.53}\text{Ga}_{0.47}\text{As}/\text{In}_{0.52}\text{Al}_{0.48}\text{As}$  heterostructure lattice matched to the InP substrate. The thickness of each layer was calculated for the continuum states to have two preferential extraction directions for the mentioned optical transitions starting from the ground state. The Schrödinger and Poisson equations were self-consistently solved using split-operator and finite element methods [18, 19], respectively.

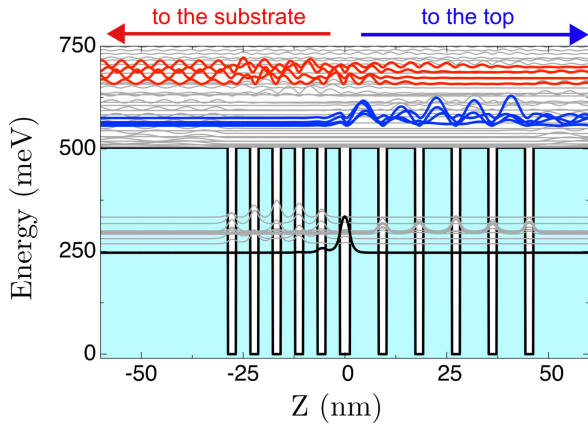
The heterostructure has a main quantum well with a 2.5 nm thickness and is embedded between two different electronic Bragg mirrors. The first Bragg mirror has five InGaAs quantum wells and five InAlAs quantum barriers with thicknesses of 2.0 nm and 3.5 nm, respectively. The second electronic Bragg mirror is composed of five 2.0 nm thick quantum wells and five 7.0 nm thick barriers. The main QW is n-doped with  $1.9 \cdot 10^{18} \text{ cm}^{-3}$ . The heterostructure is repeated 20 times separated by 30.0 nm thick InAlAs spacers. The entire active region is embedded between two n-doped InGaAs contact layers with  $2.0 \cdot 10^{18} \text{ cm}^{-3}$ .

The sample was grown by using molecular beam epitaxy and processed into  $400 \times 400 \mu\text{m}$  mesas by chemical wet-etching photolithography. Due to the intersubband transition selection rule, a 45-degree facet was polished at the detector edge for proper light coupling [16]. The contact layers were covered with evaporated Ti/Au for ohmic contact. The optical characterisation was carried out by Fourier transform infrared spectroscopy (Thermo Nicolet 6700).

## 3. Results and discussions

The electronic conduction band profile for one period of the active region is presented in Fig. 2. The ground state (black line) is localised mainly in the main quantum well with an energy of 247.0 meV. Above the ground state, the first miniband (grey lines) starting at 268.8 meV is produced by the superlattices that surround the main quantum well. The blue lines in the continuum represent the leaky electronic states with a preferential direction to flow to the right (to the top of the mesa). The leaky electronic states coloured with red lines present a preferential direction to the left (to the substrate). This heterostructure generates a positive photocurrent signal when the incident photon promotes an optical transition from the ground state to the blue leaky electronic states with the preferential direction to flow to the right. On the other hand, a negative photocurrent is obtained when the incident photon induces an optical transition to the red leaky electronic states. The donor impurities lead to a Fermi energy at 77 K equalling 273.0 meV, which means the ground state and the first state of the miniband are populated.

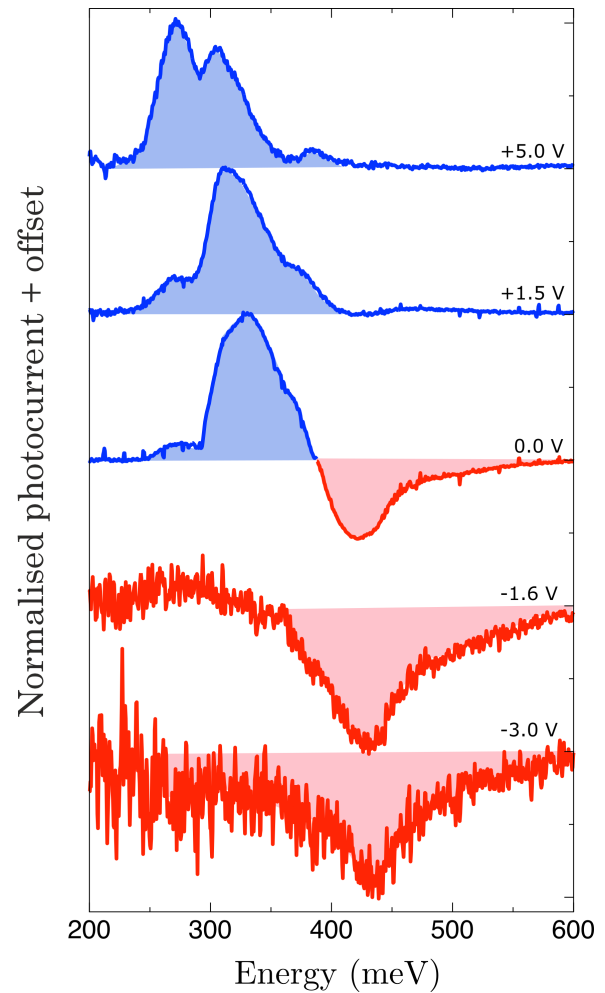
The normalised photocurrent spectra measured for several bias voltages at 77 K are depicted in Fig. 3 and present two distinct characteristics depending on the applied bias voltage: dual-colour or single-colour detection. The dual-colour detection is reached on the null bias voltage



**Fig. 2.** Conduction band profile and electronic probability density for the InGaAs/InAlAs heterostructure formed by one thicker main quantum well surrounded by two superlattices. The black line represents the ground state localised mainly in the thicker quantum well. Each superlattice was designed to work as a quantum Bragg mirror for a specific energy range. The continuum states present two specific energy ranges in which the wavefunctions of the states are localised in one direction and extended in the opposite direction. The blue lines in the continuum represent the quasi-BICs with a preferential direction for electron extraction to the right (top of the mesa), while the red lines are the quasi-BICs with a preferential electronic escape to the left (substrate).

(photovoltaic mode) or on low bias voltage regime, while the single-colour detection occurs on higher voltage regime (photoconductive mode). The positive photocurrent (blue line) indicates that the photoexcited electrons are flowing to the top of the mesa and the negative one (red line) means the electronic current is flowing to the substrate. At photovoltaic mode, the photocurrent spectrum presents one positive peak at 340 meV (3.6  $\mu\text{m}$ ) and one negative peak around 430 meV (2.9  $\mu\text{m}$ ). These results confirm that the quantum Bragg mirrors are tuning the leaky electronic states, giving rise to preferential paths for electrons to escape. By applying bias voltage, the switch from dual-colour to single-colour occurs because the bias voltage induces an extra preferential direction for the electrons to flow. Once the bias voltage surpasses a threshold value, the current starts to flow in a single direction. In our detector, the positive photocurrent is dominant for bias voltage above +1.5 V, while only negative photocurrent is detected for bias voltage below -1.6 V. Each photocurrent spectrum was normalised separately by the value of its higher peak. An energy peak around 270 meV (4.6  $\mu\text{m}$ ) emerges when positive bias is applied, attributed to transitions starting from the miniband states of the left side superlattice that lies above the ground state. The miniband is populated when bias voltage is applied and that gives rise to the second peak in the photocurrent spectrum. The third peak energy at 380 meV with small intensity emerges in the photocurrent spectrum when +5 V is applied, being related to the optical transition from the ground state to the quasi-BIC with an energy of 640 meV with respect to the bottom of the quantum well.

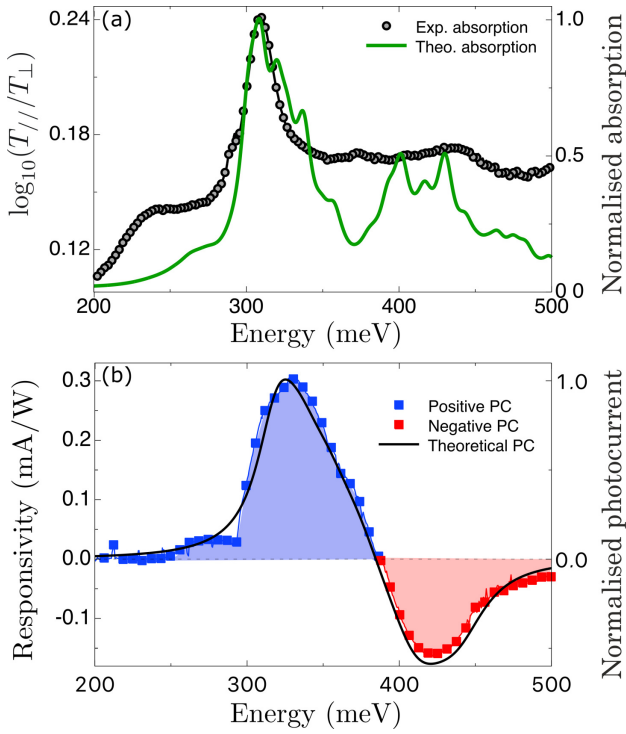
Figure 4(a) presents the comparison between the experimental absorption spectrum measured at 77 K and the theoretical absorption spectrum. The absorption was calculated using the Fermi golden rule with FWHM equal to 10%. The ground state and the first state of the miniband



**Fig. 3.** Normalised photocurrent spectra of the dual-colour QBMD as a function of applied bias voltages. The blue (red) line represents the positive (negative) photocurrent response. In photovoltaic mode, the photocurrent spectrum presents the dual-colour regime, with a positive peak at 340 meV and a negative one around 430 meV. In the photoconductive mode, the photocurrent spectrum is shifted to detect only the positive or negative peaks (single-colour regime). The positive peak is dominant for positive bias above 1.5 V, while the negative one is under -1.6 V.

were considered as the initial states for the optical transitions. The experimental absorption spectrum has one major peak at 310 meV with a lower energy shoulder around 245 meV and a plateau with a subtle peak around 435 meV. The calculation shows that the major (subtle) peak comes from optical transitions between the ground state and the blue (red) quasi-BICs, while the lower energy shoulder is related to the optical transition starting from the miniband.

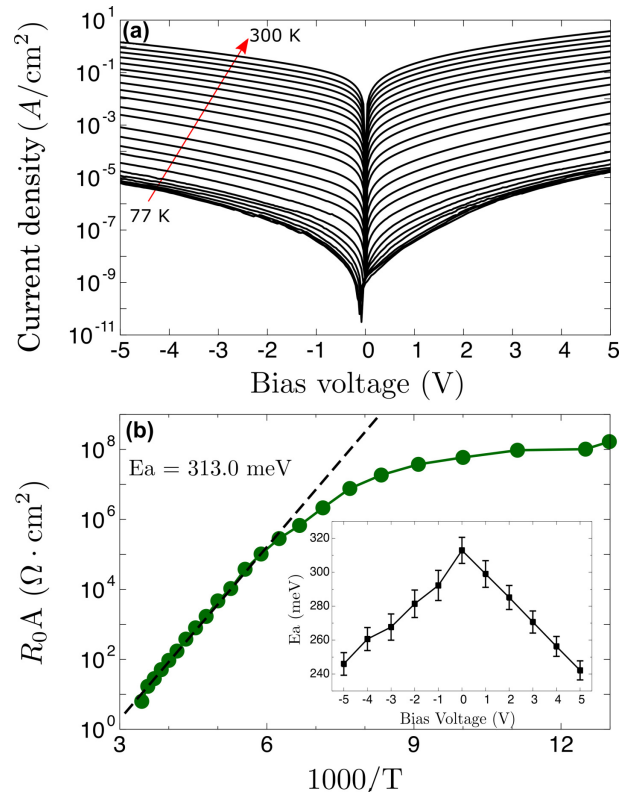
The theoretical photovoltaic photocurrent spectrum superimposed on the photocurrent measurement is presented in Fig. 4(b). The photocurrent spectrum was calculated using the theory of coherent electron emission in a quantum well heterostructure [20] and considering only the ground state as the initial state of the transition. The positive signal means that the photoexcited electron is flowing to the right side of the heterostructure (to the top of the mesa), and the negative one implies the electron moving to the left side (to the substrate). The normalised theoretical photocurrent spectrum shows a very good



**Fig. 4.** The normalised absorption spectrum measured at 77 K superimposed on the theoretical one. The experimental absorption spectrum presents two peaks, one at 310 meV and another at 435 meV, and a 250 meV shoulder. The theoretical absorption was calculated considering the ground state and the first state of the miniband as initial states for the optical transitions. The peaks at 310 meV and 430 meV are related to the optical transitions from the ground state to the blue and red quasi-BICs, respectively. The 250 meV shoulder results from the optical transition starting from the first state of the miniband (a). The comparison between the experimental photovoltaic photocurrent spectrum measured at 77 K with the theoretical one. The photovoltaic photocurrent spectrum was simulated considering the electron initially confined in the ground state (b).

agreement with the experimental one. Besides matching the positive and negative peaks, the theoretical photocurrent also correctly shows at which photon energy the signal-inversion occurs.

The dark current density-voltage ( $J$ - $V$ ) curves of the dual-colour QBMD measured between 77 K and 300 K are shown in Fig. 5(a). The thermal activation energy [21] is determined from the product between the differential resistance ( $R_0$ ), obtained from the dark current density, and the area of the mesa ( $A$ ). The  $R_0A$  vs.  $1000/T$  for zero bias is presented in Fig. 5(b). The highest value is  $1.6 \cdot 10^8 \Omega \cdot \text{cm}^2$  at 77 K and the lowest is  $6.3 \Omega \cdot \text{cm}^2$  at 300 K. The activation energy ( $E_a$ ) is determined using the Arrhenius plot at the high-temperature regime and its value as a function of the bias voltage can be seen in the inset in Fig. 5(b). The maximum value occurs for null bias (313.0 meV) and it decreases with the applied bias voltage, reaching 242.1 meV for +5.0 V and 245.9 meV for -5.0 V. Considering that the Fermi energy and the thermal activation energy are 273.0 meV and 313.0 meV, respectively, at null bias voltage, the threshold of the continuum states starts at 587.0 meV, which means that the conduction band offset was virtually increased by 84.0 meV due to the presence of the superlattices [22].



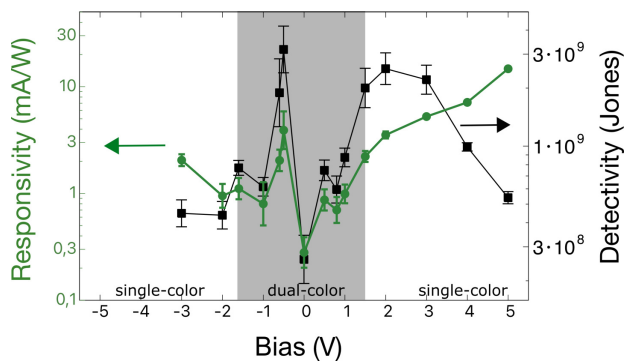
**Fig. 5.** The dark current density curves of the dual-colour QBMD measured in the range of 77 K to 300 K (a). The product between the differential resistance at null bias and the area of the mesa as a function of the inverse temperature. The differential resistance was calculated from the dark current density curves. This product has an exponential decrease with the increase in temperature. The estimated thermal activation energy, in the high-temperature regime using the Arrhenius plot, was 313.0 meV. In the inset, the thermal activation energies as a function of bias voltage are shown. The highest value occurs at null bias and decreases with bias voltage (b).

Figure 6 shows the figures of merit (peak responsivity and specific detectivity) of the QBMD as a function of the bias voltage at 77 K. Usually, the peak responsivity in QWIPs is estimated following the methodology presented by Levine [21], but this methodology only considers single-colour detection. Both peaks (positive and negative amplitudes) need to be considered to estimate the peak responsivity in the dual-colour regime. Therefore, Levine's equation needs to be modified to include the dual-colour regime.

The peak responsivity was calculated by considering

$$\mathfrak{R}_P^0 = \frac{I_P}{\gamma \left[ \int_{\lambda_1}^{\lambda_2} \bar{R}(\lambda) W(\lambda) d\lambda + \int_{\lambda_3}^{\lambda_4} \bar{R}(\lambda) W(\lambda) d\lambda \right]}, \quad (1)$$

where  $\gamma = \sin^2(\Omega/2) A_D C_F \cos \theta$ ,  $A_D$  is the mesa area,  $\Omega$  is the field of view (FOV) angle,  $\theta$  is the angle of incidence,  $C_F$  is the coupling factor,  $I_P$  is the integrated photocurrent,  $W(\lambda)$  is the blackbody spectral radiation density,  $\bar{R}(\lambda)$  is the normalised photocurrent spectrum, and  $\lambda_{1(3)}$  and  $\lambda_{2(4)}$  are the FWHM for each peak in the photocurrent spectrum. The integrated photocurrent ( $I_P$ ) was measured with a lock-in amplifier and pre-amplifier using a calibrated blackbody source at 800 °C. In the dual-colour regime measured at



**Fig. 6.** The figures of merit (peak responsivity and specific detectivity) of the dual-colour QBMD at 77 K as a function of applied bias voltage. The grey rectangle highlights the bias range for the dual-colour operation regime. The peak responsivity (green circles) presents the lowest value in the dual-colour regime, and the highest value occurs for positive single-colour at +5.0 V. The specific detectivity (black squares) presents the same characteristic as the peak responsivity, but the highest value occurs for a positive single-colour at +2.0 V.

77 K, the peak responsivity at photovoltaic mode is 0.3 mA/W and the highest peak responsivity is 3.9 mA/W at  $-0.5$  V applied bias voltage. For the single-colour mode, the photocurrent spectrum presents only one peak, the positive peak for positive bias voltage and negative peak for negative bias voltage. The highest responsivity for the positive peak is 14.2 mA/W at +5.0 V and 2.1 mA/W for the negative peak at  $-1.5$  V. The authors' previous QBMDs [24] showed better values for the peak responsivity (photovoltaic or photoconductive modes) than this dual-colour QBMD. The authors attribute the low responsivities encountered for the dual-colour device to the incomplete confinement of the wavefunction of the BIC which leads to a low oscillator strength for this optical transition. An optimization of the thicknesses of the superlattices should improve the confinement of the BIC and promptly increase the peak responsivity.

The specific detectivity (black squares in Fig. 6) was determined from the noise current measured with the lock-in amplifier [23]. The noise current was measured with the QBMD inside a heat shield and the modulation frequency and bandwidth were set up to 595 Hz and 1 Hz, respectively. For the dual-colour regime, the specific detectivity at photovoltaic mode is  $2.5 \cdot 10^8$  Jones and the highest value achieved is  $3.2 \cdot 10^9$  Jones for an applied bias voltage of  $-0.5$  V. In a single-colour mode, the highest specific detectivity for the positive and negative peaks were  $2.6 \cdot 10^9$  Jones at +2.0 V and  $7.7 \cdot 10^8$  Jones at  $-1.6$  V, respectively. These results are comparable with our previous QBMDs [11, 15, 24, 25].

#### 4. Conclusions

In conclusion, the continuum states of the heterostructure were tailored by bandgap engineering giving the quasi-BICs a preferential direction for electron extraction (towards the top of the mesa or towards the substrate). In the photovoltaic mode, the photocurrent spectrum has a positive peak at 340 meV and a negative one around 430 meV originating from optical transitions between the ground state and the quasi-BICs. The dual-

colour detection is shifted into a single-colour detection under the applied bias voltage. To detect only the positive peak, a voltage bias above +1.5 V is required, while the negative peak demands a bias voltage below  $-1.6$  V. In the dual-colour mode, the peak responsivity and specific detectivity were 0.3 mA/W and  $2.5 \cdot 10^8$  Jones, respectively. For a single-colour mode, the highest peak responsivity and specific detectivity for the positive peak were 14.2 mA/W at +5.0 V and  $2.6 \cdot 10^9$  Jones at +2.0 V, while for the negative peak, they were 2.1 mA/W at  $-3.0$  V and  $7.7 \cdot 10^8$  Jones at  $-1.6$  V. In summary, a tunable electron extraction direction was achieved by using the electronic quasi-BIC (or leaky electronic state) concept. Depending on the applied bias voltage, the active region detects simultaneously or distinctively two spectral ranges, demonstrating that the QBMD can also be applied to a multi-colour infrared detection. The next step is the structural and doping optimization of the dual-colour QBMD to improve its figures of merit (responsivity and detectivity) and, consequently, be competitive with traditional QWIPs.

#### Authors' statement

Research concept and design, G.M.P.; collection and/or assembly of data, P.H.P., V.B.S., R.M.S.K.; data analysis and interpretation, G.M.P., P.H.P., M.P.P. and P.L.S.; writing the article, G.M.P. and P.H.P.; critical revision of the article, R.M.S.K., M.P.P., P.L.S.; final approval of article, G.M.P. and P.L.S.

#### Acknowledgements

The authors thank CAPES (8887.387672/2019/00 and 8887.513331/2020-00), CNPq, FAPERJ (E-26/203.000182/2019, E-26/010.000980/2019, E-26/210.298/2019, E-26/010.001805/2019 and E-26/210.321/2022), and FINEP for the financial support.

The authors are grateful to Claire Gmachl and Deborah Sivco from Princeton University for discussions and the growth of the sample and Alain Quivy's group from Universidade de São Paulo for the processing of the devices.

#### References

- [1] Hsu, C. W., Zhen, B., Stone, A. D., Joannopoulos, J. D. & Soljacic, M. Bound states in the continuum. *Nat. Rev. Mater.* **1**, 16048 (2016). <https://doi.org/10.1038/natrevmats.2016.48>
- [2] Azzam, S. I. & Kildishev, A. V. Photonic bound states in the continuum: from basics to applications. *Adv. Opt. Mater.* **9**, 2001469 (2021). <https://doi.org/10.1002/adom.202001469>
- [3] Hsiao, H. H., Hsu, Y. C., Liu, A. Y., Hsieh, J. C. & Lin, Y. H. Ultrasensitive refractive index sensing based on the quasi-bound states in the continuum of all-dielectric metasurfaces. *Adv. Opt. Mater.* **10**, 2200812 (2022). <https://doi.org/10.1002/adom.202200812>
- [4] Sun, K. et al. 1D quasi-bound states in the continuum with large operation bandwidth in the  $\omega$  k space for nonlinear optical applications. *Photonics Res.* **10**, 1575–1581 (2022). <https://doi.org/10.1364/PRJ.456260>
- [5] Kodigala, A. et al. Lasing action from photonic bound states in continuum. *Nature* **541**, 196–199 (2017). <https://doi.org/10.1038/nature20799>

- [6] Kim, M., Kee, C.-S. & Kim, S. Graphene-based fine tuning of Fano resonance transmission of quasi-bound states in the continuum. *Opt. Express* **30**, 30666–30671 (2022). <https://doi.org/10.1364/OE.468890>
- [7] Srivastava, Y. K. et al. Terahertz sensing of 7 nm dielectric film with bound states in the continuum metasurfaces. *Appl. Phys. Lett.* **115**, 151105 (2019). <https://doi.org/10.1063/1.5110383>
- [8] Xie, Y., Zhang, Z., Lin, Y., Feng, T. & Xu, Y. Magnetic quasi-bound state in the continuum for wireless power transfer. *Phys. Rev. Appl.* **15**, 044024 (2021). <https://doi.org/10.1103/PhysRevApplied.15.044024>
- [9] von Neumann, J. & Wigner, E. P. Über merkwürdige diskrete eigenwerte. in *The Collected Works of Eugene Paul Wigner* (ed. Wightman, A. S.) 291–293 (Springer, Berlin, Heidelberg, 1993). [https://doi.org/10.1007/978-3-662-02781-3\\_19](https://doi.org/10.1007/978-3-662-02781-3_19) (in German)
- [10] Capasso, F. et al. Observation of an electronic bound state above a potential well. *Nature* **358**, 565–567 (1992). <https://doi.org/10.1038/358565a0>
- [11] Penello, G. M. et al. Exploring parity anomaly for dual peak infrared photodetection. *IEEE J. Quantum Electron.* **52**, 1–6 (2016). <https://doi.org/10.1109/JQE.2016.2623271>
- [12] Guerra, L. et al. Detecting infrared radiation beyond the band offset with intersubband transitions. *IEEE Photon. Technol. Lett.* **28**, 1641–1644 (2016). <https://doi.org/10.1109/LPT.2016.2554064>
- [13] Penello, G. M. et al. Leaky electronic states for photovoltaic photodetectors based on asymmetric superlattices. *Appl. Phys. Lett.* **112**, 033503 (2018). <https://doi.org/10.1063/1.5006464>
- [14] Schneider, F. et al. Photovoltaic quantum well infrared photodetectors: The four-zone scheme. *Appl. Phys. Lett.* **71**, 246 (1997). <https://doi.org/10.1063/1.119510>
- [15] Pereira, P. H. et al. High performance dual-mode operation asymmetric superlattice infrared photodetector using leaky electronic states. *J. Appl. Phys.* **125**, 204501 (2019). <https://doi.org/10.1063/1.5093242>
- [16] Schneider, H. & Liu, H. C. *Quantum Well Infrared Photodetectors*. (Springer, 2007).
- [17] Giorgetta, F. R. et al. Quantum cascade detectors. *IEEE J. Quantum Electron.* **45**, 1039–1052 (2009). <https://doi.org/10.1109/JQE.2009.2017929>
- [18] Degani, M. H. & Maialle, M. Z. Numerical calculations of the quantum states in semiconductor nanostructures. *J. Comput. Theo. Nanosci.* **7**, 454–473 (2010). <https://doi.org/10.1166/jctn.2010.1380>
- [19] Pereira, P. H. et al. Role of structural parameters on the leaky electronic states in the continuum of superlattice structures. *J. Integr. Circuits Syst.* **15**, 1 (2020). <https://doi.org/10.29292/jics.v15i1.108>
- [20] Schönbein, C., Schneider, H. & Walther, M. Coherent carrier propagation in the continuum of asymmetric quantum-well structures. *Phys. Rev. B* **60**, R13993 (1999). <https://doi.org/10.1103/PhysRevB.60.R13993>
- [21] Levine, B. F. Quantum-well infrared photodetectors. *J. Appl. Phys.* **74**, R1 (1993). <http://dx.doi.org/10.1063/1.354252>
- [22] Takagi, T., Koyama, F. & Iga, K. Electron-wave reflection by multi-quantum barrier in n-GaAs/i-AlGaAs/n-GaAs tunneling diode. *Appl. Phys. Lett.* **59**, 2877 (1991). <https://doi.org/10.1063/1.105839>
- [23] Kouh, T., Kemiktarak, U., Basarir, O., Lissandrello, C. & Ekinci, K. Measuring gaussian noise using a lock-in amplifier. *Am. J. Phys.* **82**, 778 (2014). <https://doi.org/10.1119/1.4873694>
- [24] Penello, G. M. et al. Progress in symmetric and asymmetric superlattice quantum well infrared photodetectors. *Ann. Phy. (Berl.)* **531**, 1800462 (2019). <https://doi.org/10.1002/andp.201800462>
- [25] Pereira, P. Quantum Well Infrared Photodetector For The Swir Range. in *Developments and Advances in Defense and Security* (eds. Rocha, A. & Pereira, P.) 363–370 (Springer, 2020). [https://doi.org/10.1007/978-981-13-9155-2\\_29](https://doi.org/10.1007/978-981-13-9155-2_29)